PROCEEDINGS OF SCIENCE

Unique Properties of Cosmic Rays: Results from the Alpha Magnetic spectrometer

V. Choutko[a,*] **and Q. Yan**[a]

[a] *Massachusetts Institute of Technology (MIT), Cambridge, Massachusetts 02139, USA*

E-mail: choutko@mit.edu, qyan@cern.ch

We report the properties of cosmic ray nuclei from protons to nickel (Z=1–14, 16, 26, and 28) in the rigidity range from 2 GV to 3 TV collected by the Alpha Magnetic Spectrometer on the International Space Station from May 19, 2011 to May 6, 2021. We found that the primary cosmic rays He-C-O-Fe-Ni, and Ne-Mg-Si-S belong to two different classes of cosmic rays. We also found that the secondary cosmic rays Li-Be-B and F belong to another two different classes of cosmic rays.The rigidity dependences of the secondary cosmic rays and the primary cosmic rays are distinctly different. In particular, above ~ 200 GV the secondary cosmic rays harden twice as much as the primary cosmic rays. The third group of cosmic rays N, Na, and Al can be described as linear combinations of primary (O, Si) and secondary (B, F) cosmic rays. Compared with O and Si, the primary cosmic rays C, Ne, Mg, and S were found to have secondary component, similar to N, Na, and Al. As a result, the C/O, N/O, Ne/Si, Na/Si, Al/Si, Mg/Si, and S/Si abundance ratios at the source are directly determined independent of cosmic ray propagation. Finally, we found that the lightest and most abundant primary proton cosmic rays have two components, the first being with the same rigidity dependence as He-C-O-Fe-Ni and the second with rigidity spectral index softer than the first one by $\Delta_{p/He} = 0.30 \pm 0.01$.

27th European Cosmic Ray Symposium - ECRS
25-29 July 2022
Nijmegen, the Netherlands

*Speaker

PoS(ECRS)012

1. Introduction

The Alpha Magnetic Spectrometer (AMS) is a precision magnetic spectrometer on the International Space Station (ISS) conducting a unique, long-duration mission of fundamental physics research in space. The physics objectives include precise studies of the origins of dark matter, antimatter, and cosmic rays as well as the exploration of new phenomena [1].

2. AMS Detector

The layout of the detector is shown in Fig. 1. The key elements are the permanent magnet [2], the silicon tracker [3], four planes of time of flight (TOF) scintillation counters [4], the array of anticoncidence counters (ACCs) [5], the transition radiation detector (TRD) [6], the ring imaging Čerenkov detector (RICH) [7], and the electromagnetic calorimeter (ECAL) [8]. The AMS coordinate system is concentric with the magnet. The x axis is parallel to the main component of the magnetic field. The (y-z) plane is the bending plane. Above, below, and downward- going refer to the AMS coordinate system. The central field of the magnet is 1.4 kG. Before flight, the field was measured in 120 000 locations to an accuracy of better than 2 G. On orbit, the magnet temperature varies from −3 to +20°C. The field strength is corrected with a measured temperature dependence of −0.09‰/°C.

The tracker has nine layers, the first ($L1$) at the top of the detector, the second ($L2$) just above the magnet, six ($L3$ to $L8$) within the bore of the magnet, and the last ($L9$) just above the ECAL. $L2$ to $L8$ constitute the inner tracker. Each layer contains double-sided silicon microstrip detectors, which independently measure the x and y coordinates. The tracker accurately determines the trajectory of cosmic rays by multiple measurements of the coordinates with a resolution in each layer of 5–10 μm in the bending (y) direction for different nuclei [9]. Together, the tracker and the magnet measure the rigidity R of charged cosmic rays, with a maximum detectable rigidity of up to 3.5 TV over the 3 m lever arm from $L1$ to $L9$. Each layer of the tracker provides an independent measurement of the charge Z with a resolution of $0.1 < \sigma_Z < 0.8$ for different charge nuclei. Overall, the inner tracker has a resolution of $0.05 < \sigma_Z < 0.3$ for Z=1...28 [10].

As seen from Fig. 1, two of the TOF planes are located above the magnet (upper TOF) and two planes are below the magnet (lower TOF). The overall velocity ($\beta = v/c$) resolution has been measured to be $\sigma(1/\beta) = 0.01 - 0.04$ for different nuclei. This discriminates between upward- and downward-going particles. The pulse heights of the two upper planes are combined to provide an independent measurement of the charge with an accuracy of $\sigma_Z/Z \sim 2\%$. The pulse heights from the two lower planes are combined to provide another independent charge measurement with the same accuracy.

Cosmic ray nuclei traversing the AMS were triggered and flagged by the logical OR of any of three trigger conditions: (i) the coincidence, within 240 ns, of signals from all four TOF planes each with a pulse height above 0.5 of a minimum ionizing particle signal (MIP, Z =1) together with an absence of signals from the ACC; OR (ii) the coincidence, within 240 ns, of signals from all four TOF planes each with pulse heights above 3.5 times a MIP signal together with signals from no more than 4 (2011-2016) or 7 (2016-) out of 8 ACC sectors; OR (iii) the coincidence, within 240 ns, of 3 out of the 4 TOF layers each with pulse heights above 0.5 of a MIP signal and with

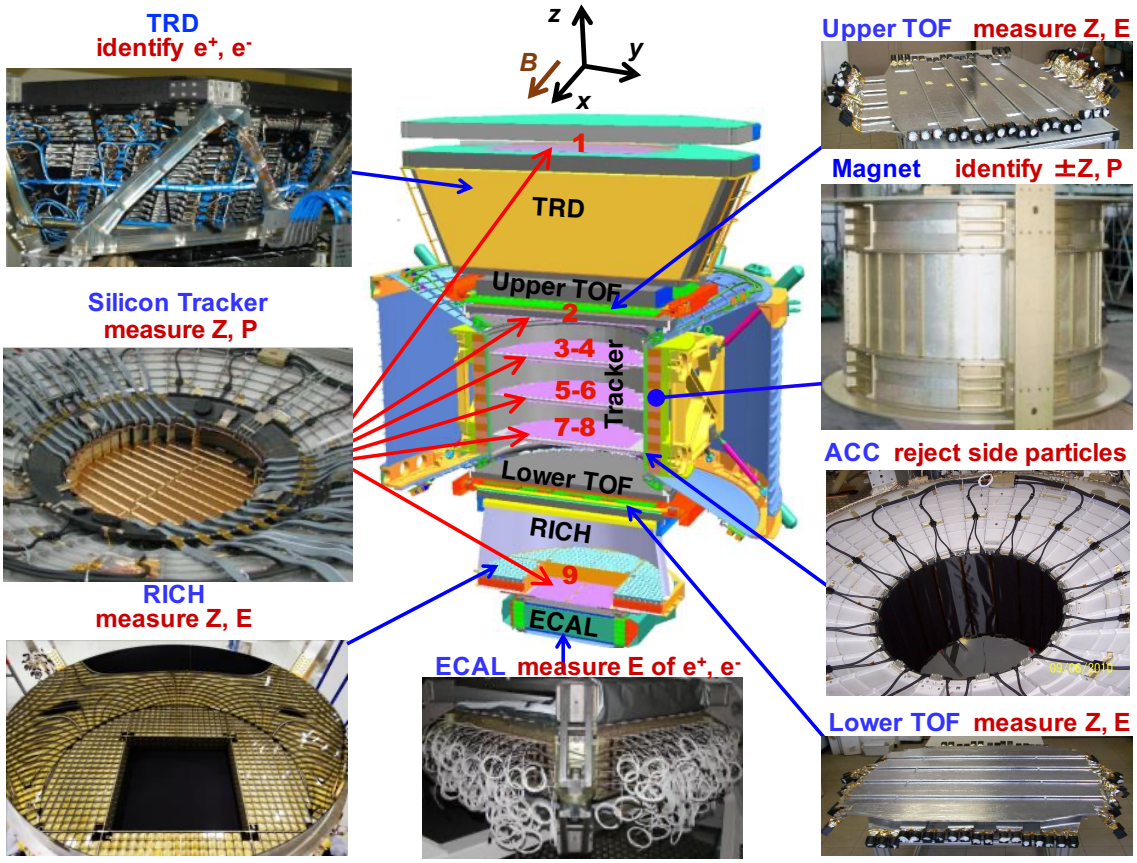

Figure 1: The AMS detector showing the main elements and their functions. AMS is a TeV precision, multipurpose particle physics magnetic spectrometer in space. It identifies particles and nuclei by their charge Z, energy E and momentum P or rigidity ($R = P/Z$), which are measured independently by the Tracker, TOF, RICH and ECAL. The ACC counters, located in the magnet bore, are used to reject particles entering AMS from the side. The AMS coordinate system is also shown. The x axis is parallel to the main component of the magnetic field and the z axis is pointing vertically.

no ACC requirement. Condition (iii) was prescaled to 1%; i.e., only 1 event out of 100 which met these conditions was passed on to the OR. The efficiency of trigger (iii) was estimated directly from the data to be above 99.9% for all rigidities using events in which 1 of the 4 TOF layers gave no signal. Trigger (iii) is then used to measure the efficiency of triggers (i) and (ii). The overall trigger efficiency has been measured to be >85% over the entire rigidity range for all nuclei.

Monte Carlo (MC) simulated events were produced using a dedicated program developed by the collaboration based on the GEANT4-10.3 package [11]. The program simulates electromagnetic and hadronic interactions [12] of particles and nuclei in the material of AMS and generates detector responses. The digitization of the signals is simulated precisely according to the measured characteristics of the electronics. The simulated events then undergo the same reconstruction as used for the data.

3. Nuclei Flux Measurements

The isotropic flux Φ_i in the ith rigidity bin $(R_i, R_i + \Delta R_i)$ is given by

$$\Phi_i = \frac{N_i}{A_i \, \epsilon_i \, T_i \, \Delta R_i} \, , \tag{1}$$

where N_i is the number of events with background subtracted and corrected for bin-to-bin migration due to finite tracker rigidity resolution, A_i is the effective acceptance obtained by simulations and corrected for small differences between the data and simulated events, ϵ_i is the measured trigger efficiency, and T_i is the collection time. Due to the geomagnetic field, the collection time increases with rigidity, reaching 2.2×10^8 s above 30 GV. Finally, the ΔR_i are chosen according to the rigidity resolution and available statistics.

Extensive studies were made of the systematic errors. These errors include the uncertainties in the background evaluation, the trigger efficiency, the acceptance calculation, the rigidity resolution function, and the absolute rigidity scale.

The main source of background comes from heavier nuclei, which interact above tracker $L1$ (thin support structures made by carbon fiber and aluminum honeycomb). The background has been estimated from the simulation using MC samples generated according to AMS flux measurements. The background is highest for the low abundant secondary nuclei like Be or F, where it can reach 15%, and is negligible for most of the primary cosmic nuclei. The uncertainty in the flux due to background subtraction is less than 1.5% up to 100 GV and 5–6% at 3.0 TV for the secondary nuclei, and is negligible for primary nuclei.

The systematic error on the flux associated with the trigger efficiency measurement is <1% over the entire rigidity range.

The systematic error of the evaluation of the effective acceptance arises mainly from the uncertainties of the inelastic cross sections of all the materials traversed by nuclei in AMS. The corresponding systematic errors are less than 2% for light nuclei ($Z \leq 6$) and are up to 4% for heavier nuclei ($Z > 6$) over the entire rigidity range.

The bin-to-bin migration of events was corrected using the unfolding procedure described in Ref. [14]. These corrections, $(N_i - \aleph_i)/\aleph_i$ where $\aleph_i$ is the number of observed events in bin i, are range typically from +20% at 2 GV to and −20% at 3 TV depending on charge magnitude of the nuclei and the flux rigidity dependence. The typical systematic error on the flux is < 4% at 2 GV, 1% from 3 GV to 300 GV and up to 4–5% at 2–3 TV.

There are two contributions to the systematic uncertainty on the rigidity scale. The first is due to the residual tracker misalignment. This error was estimated by comparing the E/p ratio for electrons and positrons, where E is the energy measured with the ECAL and p is the momentum measured with the tracker. It was found to be $1/34\,\mathrm{TV}^{-1}$ [13]. The second systematic error on the rigidity scale arises from the magnetic field map measurement and its temperature corrections. The error on fluxes due to uncertainty on the rigidity scale is less than <1% up to 200 GV and increases smoothly to 4–7% at 2–3 TV depending on the flux rigidity dependence.

4. Results

He, C, and O— Helium is next abundant cosmic ray nuclei after the proton. To study the rigidity dependence of He flux at high rigidities we fit the flux above 45 GV with a double power law function in the presence of solar modulation in the force field approximation [15]

$$\Phi = C\frac{R^2}{\hat{R}^2}\left(\frac{\hat{R}}{45\,\mathrm{GV}}\right)^{\gamma}\left[1+\left(\frac{\hat{R}}{R_0}\right)^{\Delta\gamma/s}\right]^{s} \tag{2}$$

where s quantifies the smoothness of the transition of the spectral index from γ for rigidities below the characteristic transition rigidity R_0 to $\gamma+\Delta\gamma$ for rigidities above R_0, $\hat{R} = R + \phi$, and $\phi = 0.50 \pm 0.05$ GV is the solar potential [16]. Fitting over the range 45 GV to 3 TV yields a $\chi^2/d.f. = 20/28$ with $C_{\mathrm{He}} = (950 \pm 5(\mathrm{fit}) \pm 10(\mathrm{sys}) \pm 10(\mathrm{sol})) \times 10^{-4}$ $\mathrm{m^{-2}sr^{-1}sec^{-1}GV^{-1}}$, $\gamma_{\mathrm{He}} = -2.750 \pm 0.002(\mathrm{fit}) \pm 0.003(\mathrm{sys}) \pm 0.005(\mathrm{sol})$, $\Delta\gamma_{\mathrm{He}} = 0.164^{+0.016}_{-0.017}(\mathrm{fit}) \pm 0.03(\mathrm{sys}) \pm 0.005(\mathrm{sol})$, $s = 0.04 \pm 0.01(\mathrm{fit}) \pm 0.02(\mathrm{sys}) \pm 0.01(\mathrm{sol})$, and $R_0 = 369^{+44}_{-34}(\mathrm{fit})^{+57}_{-38}(\mathrm{sys}) \pm 1(\mathrm{sol})$ GV.

The first error quoted (fit) takes into account the statistical and uncorrelated systematic errors from the He flux. The second (sys) is the error from the remaining systematic errors, namely, from the rigidity resolution function and unfolding, and from the absolute rigidity scale, with the bin-to-bin correlations properly accounted. The third (sol) is the uncertainty due to the variation of the solar potential ϕ from 0.45 GV to 0.55 GV. Figure 2 (left panel) shows the He flux together with the fit results.

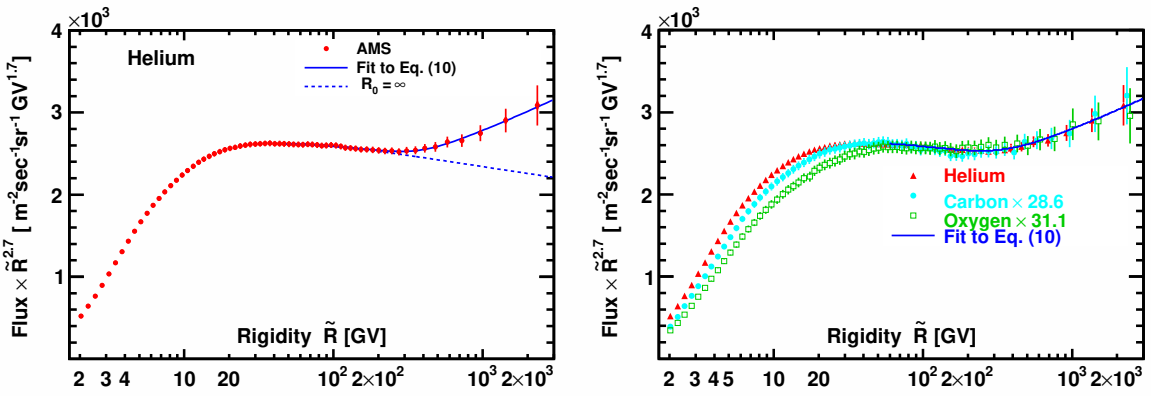

Figure 2: Left panel: The AMS helium flux multiplied by $\tilde{R}^{2.7}$ as a function of rigidity R. The solid curve indicates the fit of Eq. (2) to the data. For illustration, the dashed curve uses the same fit values but with R_0 set to infinity. Right Panel: The AMS He, C, and O fluxes. The solid curve indicates the combined fit of Eq. (2) to the data. As seen, at high rigidities, the rigidity dependence of He,C, and O fluxes is identical.

Previously, AMS found that He, C, and O fluxes have identical rigidity dependence above 60 GeV and deviate from single power law at high rigidities [17]. To examine this in detail we perform simultaneous fit of the latest AMS He, C, and O fluxes with Eq. (2) with common parameters s, γ, R_0, $\Delta\gamma$. The fit yields $C_{\mathrm{He}} = (950 \pm 5) \times 10^{-4}$ $\mathrm{m^{-2}sr^{-1}s^{-1}GV^{-1}}$, $C_{\mathrm{C}} = (31 \pm 1) \times 10^{-4}$ $\mathrm{m^{-2}sr^{-1}s^{-1}GV^{-1}}$, $C_{\mathrm{O}} = (33 \pm 1) \times 10^{-4}$ $\mathrm{m^{-2}sr^{-1}s^{-1}GV^{-1}}$, $\gamma_{\mathrm{HeCO}} = -2.760 \pm 0.002$, $\Delta\gamma_{\mathrm{HeCO}} = 0.173 \pm 0.015$, $s = 0.05 \pm 0.015$, and $R_0 = 330^{+40}_{-30}$ GV, where only (fit) errors are shown. The

He, C, and O fluxes together with the fit results are shown in Fig. 2, right panel. As seen, at high rigidities, the rigidity dependence of He, C, and O fluxes is identical.

Ne, Mg, Si, and S— Previously, AMS found that the Ne, Mg, and Si primary cosmic ray fluxes have identical rigidity dependence above 86.5 GV and deviate from a single power law. The rigidity dependence of Ne, Mg, and Si spectra is distinctly different from the rigidity dependence of primary cosmic rays He, C, and O. This shows that the Ne-Mg-Si and He-C-O are two different classes of primary cosmic rays [18]. Using latest AMS data we found that, above 86.5 GV, the Ne/O, Mg/O, and Si/O ratios can be described by a simple power law $\propto R^{\delta}$ with $< \delta >= -0.042 \pm 0.007$.

Figure 3, left panel, shows the rigidity dependence of the latest AMS Ne, Mg, and Si fluxes compared to the rigidity dependence of the He, C, and O fluxes above 86.5 GV together with the fit result of He, C, and O fluxes and Ne, Mg, and Si fluxes with Eq. (2). As seen the rigidity dependences of Ne, Mg, and Si and He, C, and O are distinctly different.

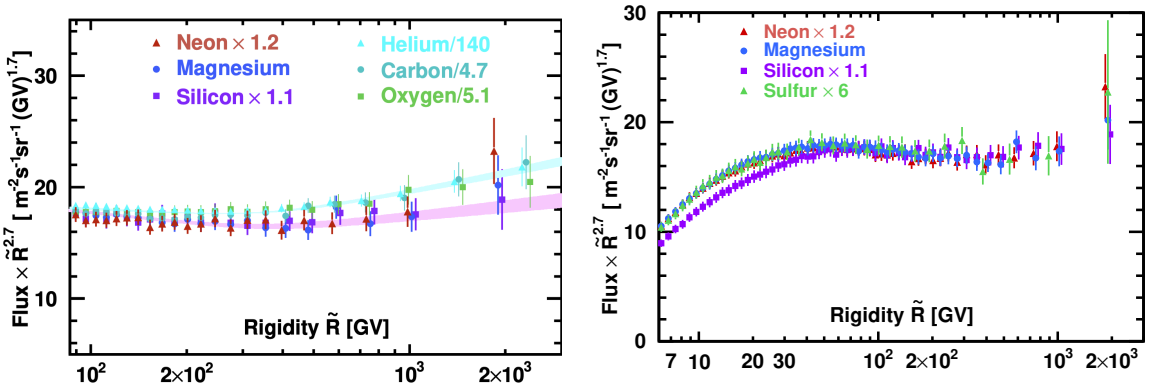

Figure 3: Left panel:The rigidity dependence of the Ne, Mg, and Si fluxes compared to the rigidity dependence of the He, C, and O fluxes above 86.5 GV. The blue solid curve shows the fit result of He, C, and O fluxes with Eq. (2). The magenta shaded area shows the fit result, including errors of Ne, Mg and Si fluxes with Eq. (2) where $\gamma_{\mathrm{NeMgSi}} + \Delta\gamma_{\mathrm{NeMgSi}} = \gamma_{\mathrm{HeCO}} + \Delta\gamma_{\mathrm{HeCO}} + < \delta >$, and $< \delta >= -0.042 \pm 0.007$. Right panel: The rigidity dependence of the Ne, Mg, Si, and S fluxes.

Figure 3, right panel, shows rigidity dependence of the latest AMS Ne, Mg, Si, and S fluxes. As seen, at high rigidities the rigidity dependence of all four fluxes is identical. To examine the S flux rigidity dependence in detail, the fits with power law functions of S/Mg and S/O flux ratios have been done and shown in Fig. 4. As seen, the rigidity dependences of S and Mg fluxes above 6 GV are very similar, and in contrast rigidity dependences of S and O fluxes above 86.5 GV are different.

Fe and Ni— Recently, AMS found that above 80.5 GV the rigidity dependence of the cosmic ray Fe flux is identical to the rigidity dependence of the primary cosmic ray He, C, and O fluxes. In particular, above 80.5 GV the Fe/O ratio is well described by a constant value of 0.155 ± 0.006 [19]. Figure 5, left panel, shows latest AMS fluxes of Fe and He together above 80.5 GV. As seen, their rigidity dependences are identical. Figure 5, right panel, shows the AMS Ni flux together with Fe flux. As seen, the rigidity dependences of Fe and Ni are also very similar.

To examine the Ni rigidity dependence in detail, a fit of the Ni/Fe fluxes ratio with a power

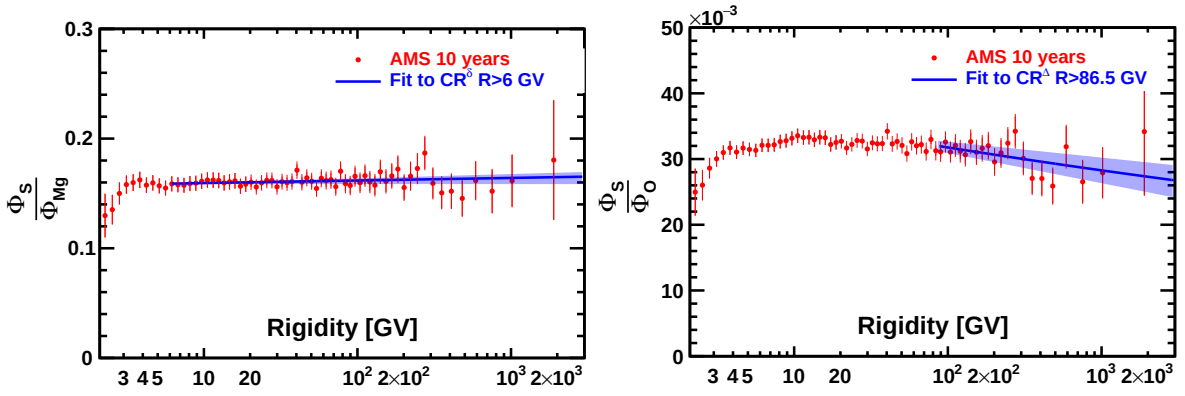

Figure 4: Left panel: The rigidity dependence of the S/Mg flux ratio together with the power law fit result CR^{δ}, $\delta = 0.006 \pm 0.006$. Right panel: The rigidity dependence of the S/O flux ratio together with the power law fit result CR^{Δ}, $\Delta = -0.05 \pm 0.02$. Blue lines and shadows show the fit results with uncertainties.

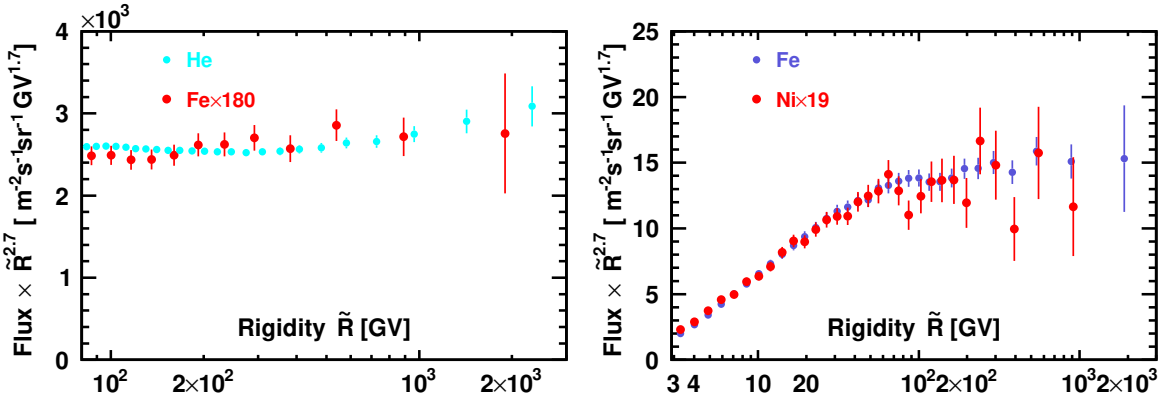

Figure 5: Left panel: The rigidity dependence of the Fe flux compared to the rigidity dependencepf the He flux above 80.5 GV. Right panel: The rigidity dependence of the Ni flux compared to the rigidity dependence of the Fe flux above 3 GV.

law CR^{δ} was performed above 3 GV, see Fig. 6. The fit yields $\delta = -0.006 \pm 0.009$ with $\chi^2/\text{dof} = 20/29$, confirming that Ni and Fe rigidity dependence is identical.

p and p/He— Protons are the most abundant cosmic rays. To study the rigidity dependence of proton flux at high rigidities we fit the flux above 45 GV with Eq. (2) in the presence of solar modulation in the force field approximation [15]. The fit yields a $\chi^2/d.f. = 22/26$ with $C_{\rm p} = (4430 \pm 2(\text{fit}) \pm 30(\text{sys}) \pm 30(\text{sol})) \times 10^{-4}$ m^{-2}sr^{-1}sec^{-1}GV^{-1}, $\gamma_{\rm p} = -2.848 \pm 0.002(\text{fit}) \pm 0.003(\text{sys}) \pm 0.007(\text{sol})$, $\Delta\gamma_{\rm p} = 0.240^{+0.013}_{-0.015}(\text{fit}) \pm 0.03(\text{sys}) \pm 0.007(\text{sol})$, $s = 0.08 \pm 0.02(\text{fit}) \pm 0.02(\text{sys}) \pm 0.01(\text{sol})$, and $R_0 = 330^{+49}_{-36}(\text{fit})^{+58}_{-48}(\text{sys}) \pm 2(\text{sol})$ GV.

Figure 7, left panel, shows the AMS latest proton flux together with the fit results. As seen, comparing with the He flux fit results, the $\gamma_{\rm p} \neq \gamma_{\rm He}$ while $\gamma_{\rm p} + \Delta\gamma_{\rm p} = -2.608^{+0.013}_{-0.015}$ is compatible with $\gamma_{\rm He} + \Delta\gamma_{\rm He} = -2.586^{+0.016}_{-0.017}$ within 1σ.

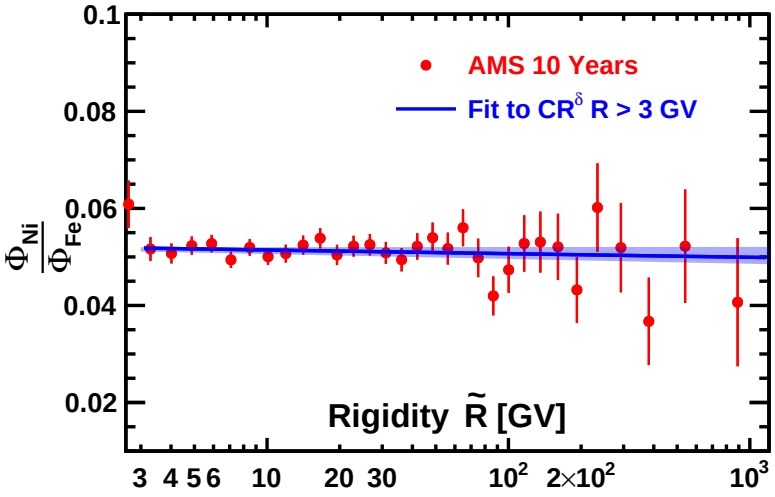

Figure 6: The rigidity dependence of the Ni/Fe flux ratio together with the power law fit result CR^{δ}, $\delta = -0.006 \pm 0.009$. Blue line and shadow show the fit results with uncertainties.

To examine this observation in detail, we fit the p/He fluxes ratio above 3.5 GV with a function

$$\frac{\Phi_{\rm p}}{\Phi_{\rm He}} = A + C \times (R/3.5\ {\rm GV})^{\Delta_{p/He}} \tag{3}$$

The fit yields a χ^2/ndf =50/58 with $A = 3.14 \pm 0.06$, $C = 3.28 \pm 0.07$, and $\Delta_{p/He} = -0.30 \pm 0.01$. Figure 7, right panel, shows the p/He flux ratio together with the fit result. As seen, the p flux has two components, the first with the same rigidity dependence as He and the second with rigidity spectral index softer by $\Delta_{p/He}$. We can use AMS data to predict asymptotic p/He ratio in kinetic energy per nucleon at high energies $(\frac{\Phi_{\rm p}}{\Phi_{\rm He}})_{k.e.\to{\rm inf}} = A/2^{\gamma+\Delta\gamma+1} = 9.52 \pm 0.38$.

Li, Be, and B— Previously AMS has reported that the Li, Be, and B secondary cosmic ray fluxes have identical rigidity dependence above 30 GV [20]. Figure 8 shows the latest AMS Li, Be, and B fluxes together with the latest He, C, and O fluxes. As seen, the three fluxes, Li, Be, and B, deviate from a single power law at high rigidities in an identical way. This behaviour of the secondary cosmic rays has also been observed in the primary cosmic rays He, C, and O, but the rigidity dependences of the primary cosmic rays and of the secondary cosmic rays are distinctly different. To study the difference of the rigidity dependence between Li, Be, and B and He, C, and O , the Li/C, Be/C, B/C and Li/O, Be/O, B/O flux ratios were fitted over 60 GV with a double power law function

$$\begin{cases} k\,(R/R_0)^{\Delta_1}, & R \le R_0\ {\rm GV}, \\ k\,(R/R_0)^{\Delta_2}, & R > R_0\ {\rm GV}. \end{cases} \tag{4}$$

The fit results are shown on Fig. 9. On average, the spectral indices of Li/C, Be/C and B/C, above $R_0 \sim 200$ GV exhibit a hardening of 0.116 ± 0.022 and the spectral indices of Li/O, Be/O and B/O, above $R_0 \sim 200$ GV exhibit a hardening of 0.176 ± 0.026. The latter number is very close

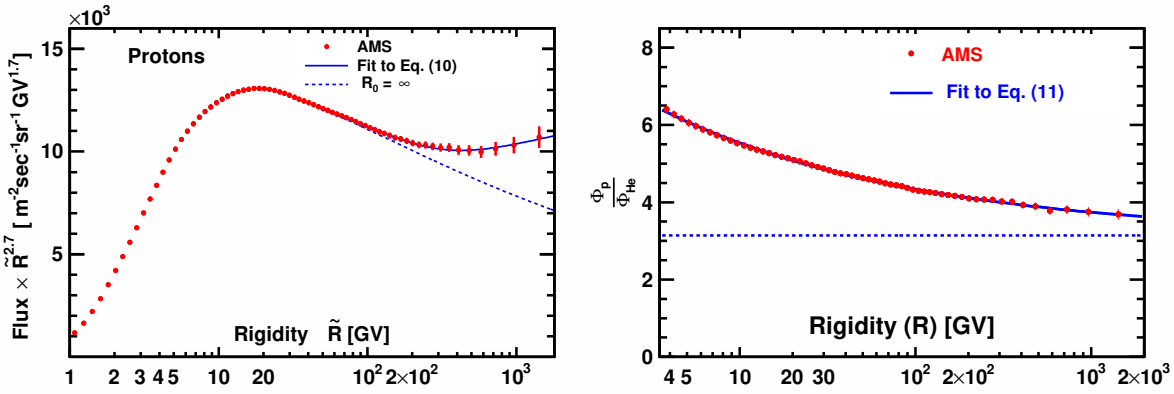

Figure 7: Left panel: The AMS helium flux multiplied by $\tilde{R}^{2.7}$ as a function of rigidity R. The solid curve indicates the fit of Eq. (2) to the data. For illustration, the dashed curve uses the same fit values but with R_0 set to infinity. Right panel: The rigidity dependence of the p/He flux ratio. The sold curve indicates the fit of Eq. (3) to the data. For illustration, the dashed curve shows the value of the constant component A.

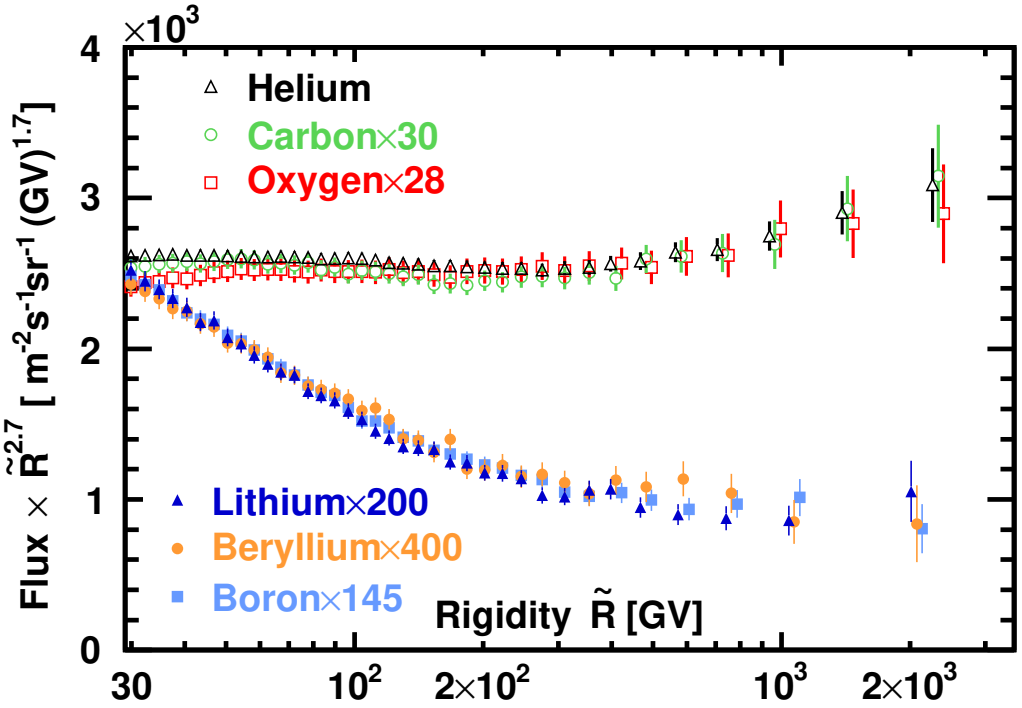

Figure 8: Comparison of the secondary cosmic ray fluxes with the AMS primary cosmic ray fluxes multiplied by $R^{2.7}$ with their total error as functions of rigidity above 30 GV. As seen, the three secondary fluxes have an identical rigidity dependence above 30 GV, as do the three primary fluxes above 60 GV.

to the hardening of the primary cosmic ray He, C, and O ($\Delta\gamma_{\mathrm{HeCO}} = 0.173 \pm 0.015$). The difference between hardening to C and to the O is due to C contains a sizeable secondary fraction (see also section below).

The AMS result shows that above ~ 200 GV the secondary cosmic rays harden twice as much

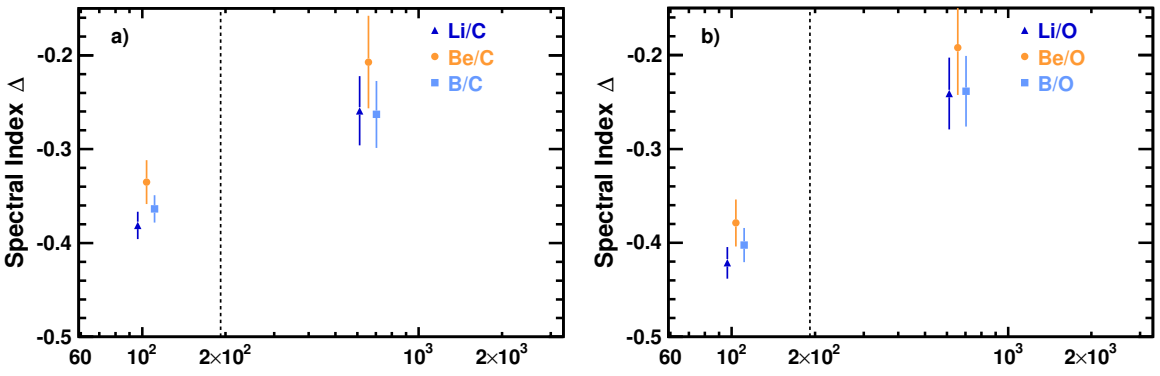

Figure 9: The AMS secondary to primary flux ratio spectral indices Δ from Eq. (4) as functions of rigidity for (a) Li/C, Be/C, and B/C and for (b) LiO, Be/O, and B/O. For (a) and (b) the vertical dashed line shows the R_0 value of 192 GV. On average, the spectral indices of Li/C, Be/C, B/C, Li/O, Be/O, and B/O exhibit a hardening above 200 GV of 0.145 ± 0.022 (a 6.5σ significance).

as the primary cosmic rays. This strongly favours the hypothesis that the hardening is related to propagation properties in the Galaxy [21]. To verify this result, the fit of flux ratio of characteristic secondary flux B to characteristic primary flux O with Eq. (2) with ϕ parameter set to zero was performed above 45 GV, see Fig 10. The fit yields $\gamma_{\mathrm{B/O}} = -0.41 \pm 0.01$, $\Delta\gamma_{\mathrm{B/O}} = 0.21 \pm 0.08$, $s = 0.05 \pm 0.04$, and $R_0 = 240 \pm 82$ GV with χ^2/ndf=24/29, again in a good agreement with $\Delta\gamma_{\mathrm{HECO}} = 0.173 \pm 0.015$.

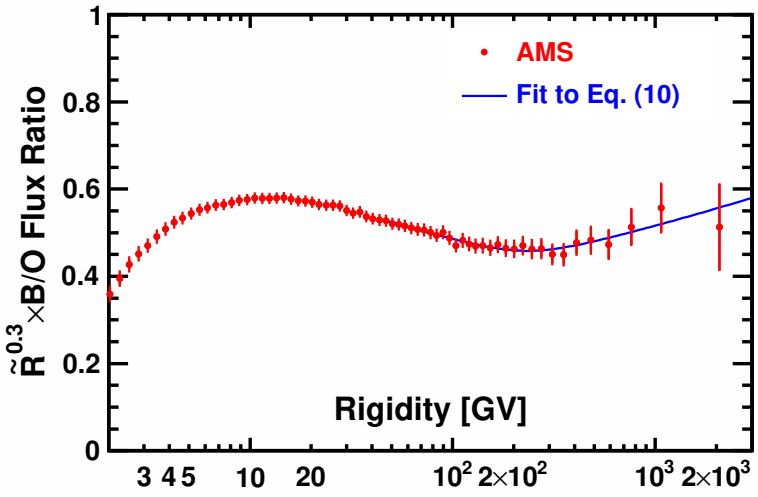

Figure 10: The AMS B/O flux ratio multiplied by $\tilde{R}^{0.3}$ as a function of rigidity R. The solid curve indicates the fit of Eq. (2) to the data.

F— AMS has reported [22] that the heavier secondary-to-primary F/Si flux ratio rigidity dependence is distinctly different from the lighter B/O (or B/C) rigidity dependence. This shows

that the secondary cosmic rays also have two classes but that the rigidity dependences of the two secondary classes are distinctly different from the rigidity dependences of the two primary classes. The variation with rigidity of the spectral index Δ of the latest AMS F/Si flux ratio was obtained by fitting it with Eq. (4) over 28.8 GV with $R_0 = 175$ GV. The fit yields $\Delta_1^{\mathrm{F/Si}} = -0.35 \pm 0.02$, and $\Delta_2^{\mathrm{F/Si}} = -0.18 \pm 0.07$ with χ^2/d.o.f.=12/16. Above 175 GV the spectral index $\Delta^{\mathrm{F/Si}}$ exhibits a hardening of 0.17 ± 0.07, compatible with the AMS results on the Li/O, Be/O, and B/O flux ratios hardening of 0.176 ± 0.026. Figure 11, left panel, shows the AMS F/Si fit results with Eq. (4) together with the AMS B/O fit results with Eq. (4), $\Delta_1^{\mathrm{B/O}} = -0.405 \pm 0.005$, and $\Delta_2^{\mathrm{B/O}} = -0.255 \pm 0.022$ with χ^2/d.o.f.=29/36. To compare the rigidity dependence of the F/Si flux ratio with the lighter secondary-to-primary B/O flux ratio in detail, the $\frac{\mathrm{F/Si}}{\mathrm{B/O}}$ ratio was computed and shown in Fig. 11, right panel. Over the entire rigidity range $\frac{\mathrm{F/Si}}{\mathrm{B/O}}$ can be fitted with Eq. (4). The fit yields $k = 0.39 \pm 0.01$, $R_0 = 9.8 \pm 0.9$ GV, $\Delta_1 = -0.052 \pm 0.010$, and $\Delta_2 = 0.0525 \pm 0.0065$ with χ^2/d.o.f.=24/46. The latest AMS result shows that above 10 GV the $\frac{\mathrm{F/Si}}{\mathrm{B/O}}$ ratio can be described by a single power law $\propto R^{\delta}$ with $\delta = 0.0525 \pm 0.0065$ (a $> 7\sigma$ difference from zero). Appendix B details additional systematic error estimation on δ from the presence of heavy secondaries in the B, O, and Si fluxes.

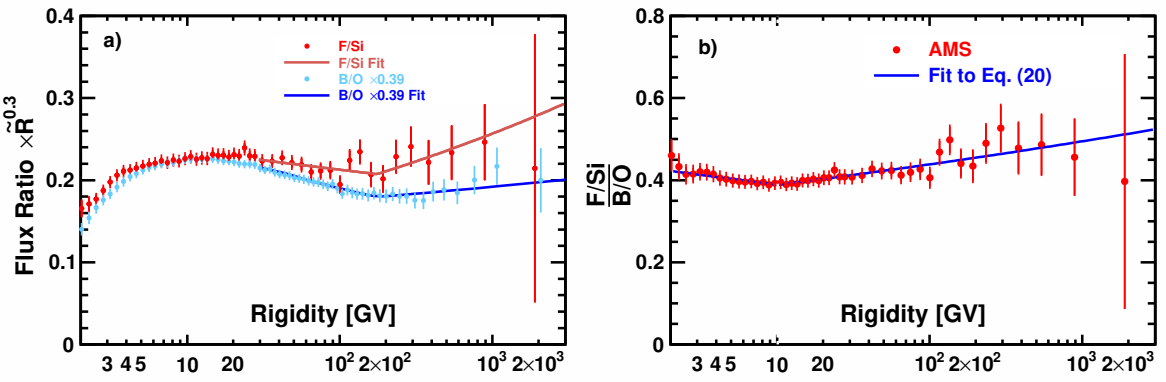

Figure 11: Left panel: The AMS F/Si flux ratio and AMS B/O flux ratio as functions of rigidity with total errors. For display purposes only, the F/Si and B/O flux ratios are multiplied by $\tilde{R}^{0.3}$ and the B/O flux ratio rescaled as indicated. The solid red and blue curves show the F/Si and B/O fit results with Eq. (4), respectively. Right panel: The AMS $\frac{\mathrm{F/Si}}{\mathrm{B/O}}$ ratio as a function of rigidity with total errors. The solid blue curve shows the fit results of Eq. (4). As seen, the rigidity dependence of F/Si and B/O flux ratios are distinctly different. Above 10 GV the $\frac{\mathrm{F/Si}}{\mathrm{B/O}}$ ratio can be described by a single power law $\propto R^{\delta}$ with $\delta = 0.0525 \pm 0.0065$ (a $> 7\sigma$ difference from zero).

Third group of cosmic rays N, Na, Al ...— AMS recently reported [23] that Na and Al, together with N, belong to a distinct cosmic ray group and are the combinations of primary and secondary cosmic rays. Similar to the N flux, which is well described by the sum of a primary cosmic ray component (proportional to the O flux) and a secondary cosmic ray component (proportional to the B flux), both the Na and Al fluxes are well described by the sums of a primary cosmic ray component (proportional to the Si flux) and a secondary cosmic ray component (proportional to the F flux). The fraction of the primary component increases with rigidity for the N, Na, and Al fluxes and becomes dominant at the highest rigidities. Figure 12 shows the latest AMS N, Na, and

Al fluxes together with the fits to the weighted sum of primary (O, Si) and secondary (B, F) fluxes.

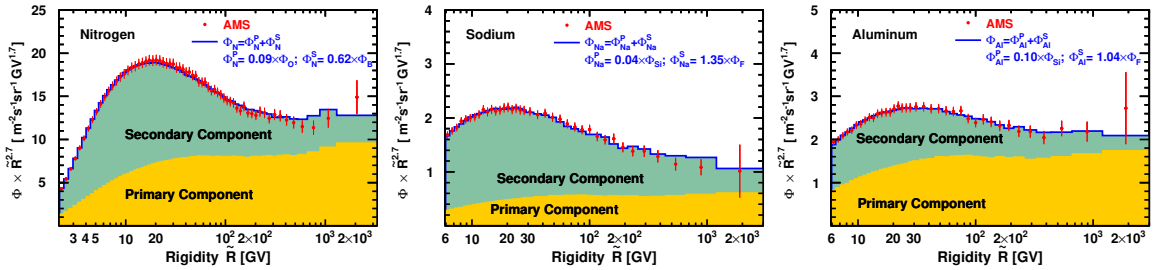

Figure 12: The latest AMS N, Na, and Al fluxes together with the fits to the weighted sum of primary (O,Si) and secondary (B,F) fluxes.

Primary cosmic rays C as well as Ne, Mg, and S are expected to have measurable secondary components [24]. To precisely determine the C, Ne, Mg, and S primary and secondary components we have fitted them as linear combinations of primary (O,Si) and secondary (B,F) fluxes.

Figure 13 shows the latest AMS C, Ne, Mg, and S fluxes together with the fits to the weighted sum of primary (O,Si) and secondary (B,F) fluxes.

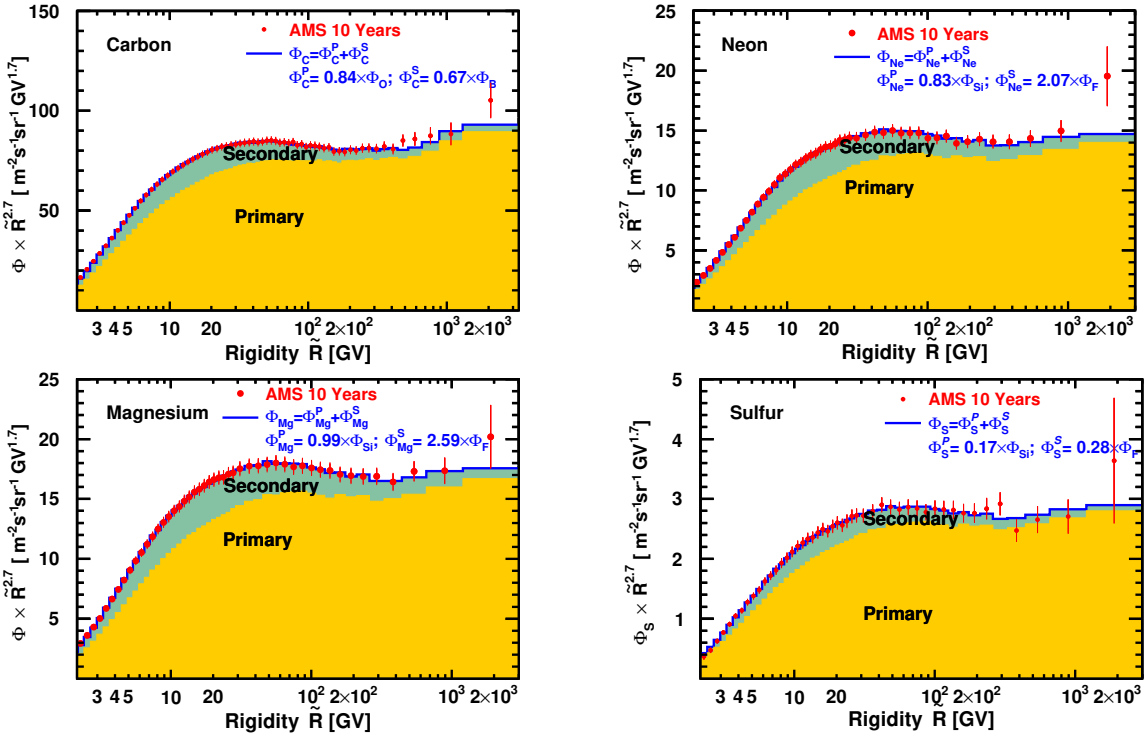

Figure 13: The latest AMS C, Ne, Mg, and S luxes together with the fits to the weighted sum of primary (O,Si) and secondary (B,F) fluxes.

Table 1 summarises the C, N, Ne, Na, Al, Mg, and S cosmic ray nuclei primary and secondary components. The C/O, N/O, Ne/Si, Na/Si, Al/Si, Mg/Si, and S/Si abundance ratios at the source are directly determined independent of cosmic ray propagation, see table 1 "Primary" column for

numerical values. Appendix A details additional systematic errors on C/O and N/O abundance ratios at the source due to presence of heavy secondaries in the B and O fluxes and Ref. [23] studies the propagation effects.

Nuclei Flux	Primary	Secondary	Secondary Fr,% 6 GV	Secondary Fr,% 2 TV
Φ_C	$(0.84 \pm 0.02) \times \Phi_O$	$(0.67 \pm 0.02) \times \Phi_B$	20±1	4±0.5
Φ_N	$(0.090 \pm 0.002) \times \Phi_O$	$(0.62 \pm 0.02) \times \Phi_B$	69±1	23±2
Φ_{Ne}	$(0.83 \pm 0.02) \times \Phi_{Si}$	$(2.07 \pm 0.14) \times \Phi_F$	24±1	5±0.5
Φ_{Na}	$(0.036 \pm 0.003) \times \Phi_{Si}$	$(1.35 \pm 0.04) \times \Phi_F$	83±2	38±12
Φ_{Mg}	$(0.99 \pm 0.03) \times \Phi_{Si}$	$(2.59 \pm 0.19) \times \Phi_F$	25±1	5±0.5
Φ_{Al}	$(0.104 \pm 0.005) \times \Phi_{Si}$	$(1.04 \pm 0.03) \times \Phi_F$	57±2	22±8
Φ_S	$(0.167 \pm 0.006) \times \Phi_{Si}$	$(0.28 \pm 0.05) \times \Phi_F$	18±3	3±1

Table 1: The C, N, and Ne, Na, Al, Mg, S cosmic ray nuclei primary and secondary components as fractions of O and B fluxes and Si and F fluxes, respectively, and their relative secondary fractions at 6 GV and 2 TV.

5. Summary

The properties of cosmic rays p, He, Li, Be, B, C, N, O, F, Ne ,Na , Mg, Al, Si, S, Fe, and Ni have been presented. We found that the primary cosmic rays He-C-O-FeNi, and Ne-Mg-Si-S belong to two different classes of cosmic rays. We also found that the secondary cosmic rays Li-Be-B and F belong to another two different classes of cosmic rays.The rigidity dependences of the secondary cosmic rays and the primary cosmic rays are distinctly different. In particular, above ~ 200 GV the secondary cosmic rays harden twice as much as the primary cosmic rays. The third group of cosmic rays N, Na, and Al can be described as linear combinations of primary (O, Si) and secondary (B, F) cosmic rays. Compared with O and Si, the primary cosmic rays C, Ne, Mg, and S were found to have secondary component, similar to N, Na, and Al. As a result, the C/O, N/O, Ne/Si, Na/Si, Al/Si, Mg/Si, and S/Si abundance ratios at the source are directly determined independent of cosmic ray propagation. Finally, we found that the lightest and most abundant primary proton cosmic rays have two components, the first being with the same rigidity dependence as He-C-O-Fe-Ni and the second with rigidity spectral index softer than the first one by $\Delta_{p/He} = 0.30 \pm 0.01$. In conclusion, Fig. 14 shows sixteen AMS nuclei fluxes, He to Ni, together. Note, that results for S and Ni fluxes, and composition of Ne, Mg, Si, S, and C fluxes as linear combinations of primary and secondary components are preliminary, please refer to future AMS publications.

6. Comparison of AMS results with other measurements

To compare AMS results with other measurements we have converted our measurements as functions of kinetic energy per nuclei (GeV/n). Figure 15 shows the AMS proton flux and p/He ratio together with other measurements and AMS p/He prediction for high energies. Figure 16 shows the comparison of the AMS results with other measurements and with the predictions of the most recent cosmic ray model GALPROP–HELMOD [25] for Z=2–9. Figure 17 shows the comparison

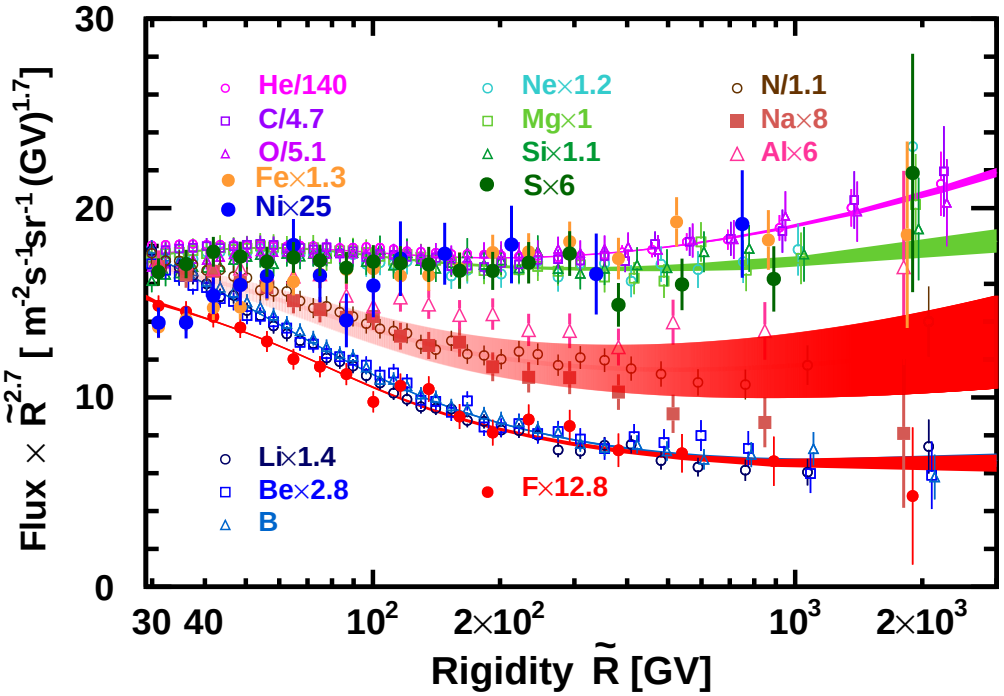

Figure 14: The fluxes of cosmic nuclei measured by AMS as functions of rigidity from Z=2–14, Z=16, Z=26, and Z=28 above 30 GV. As seen, there are two classes of primary cosmic rays, He-C-O-Fe-Ni and Ne-Mg-Si-S, and two classes of secondary cosmic rays, Li-Be-B and F. Nitrogen (N), sodium (Na), and aluminum (Al), belong to a distinct group and are the combinations of primary and secondary cosmic rays. The shaded tan band on N, Na, and Al is to guide the eye.

of the AMS results with other measurements and with the predictions of the most recent cosmic ray model GALPROP–HELMOD for Z=10–14, Z=16, Z=26, and Z=28. As seen, AMS results are often different from other measurements both in accuracy and functional dependence.

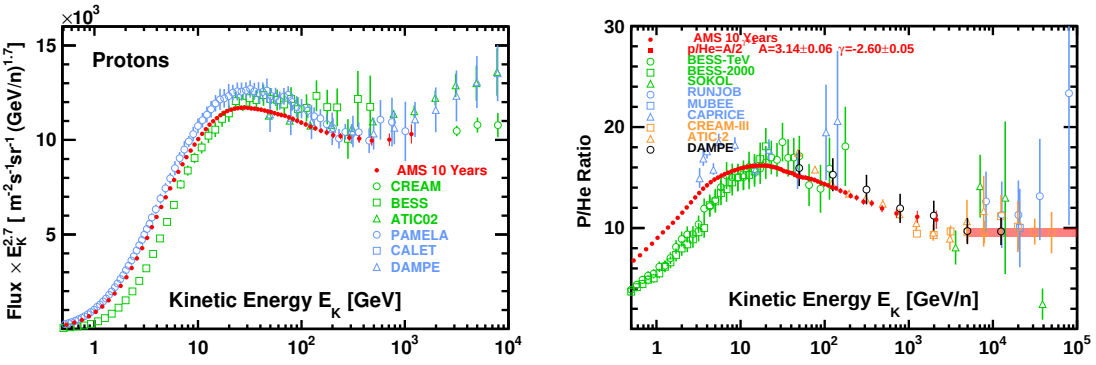

Figure 15: Left panel: AMS proton flux together with other measurements [26, 27, 33–36] as a function of kinetic energy. Right panel: The AMS p/He ratio together with other measurements [26–34, 36, 37] and AMS p/He prediction for high rigidities as a function of kinetic energy.

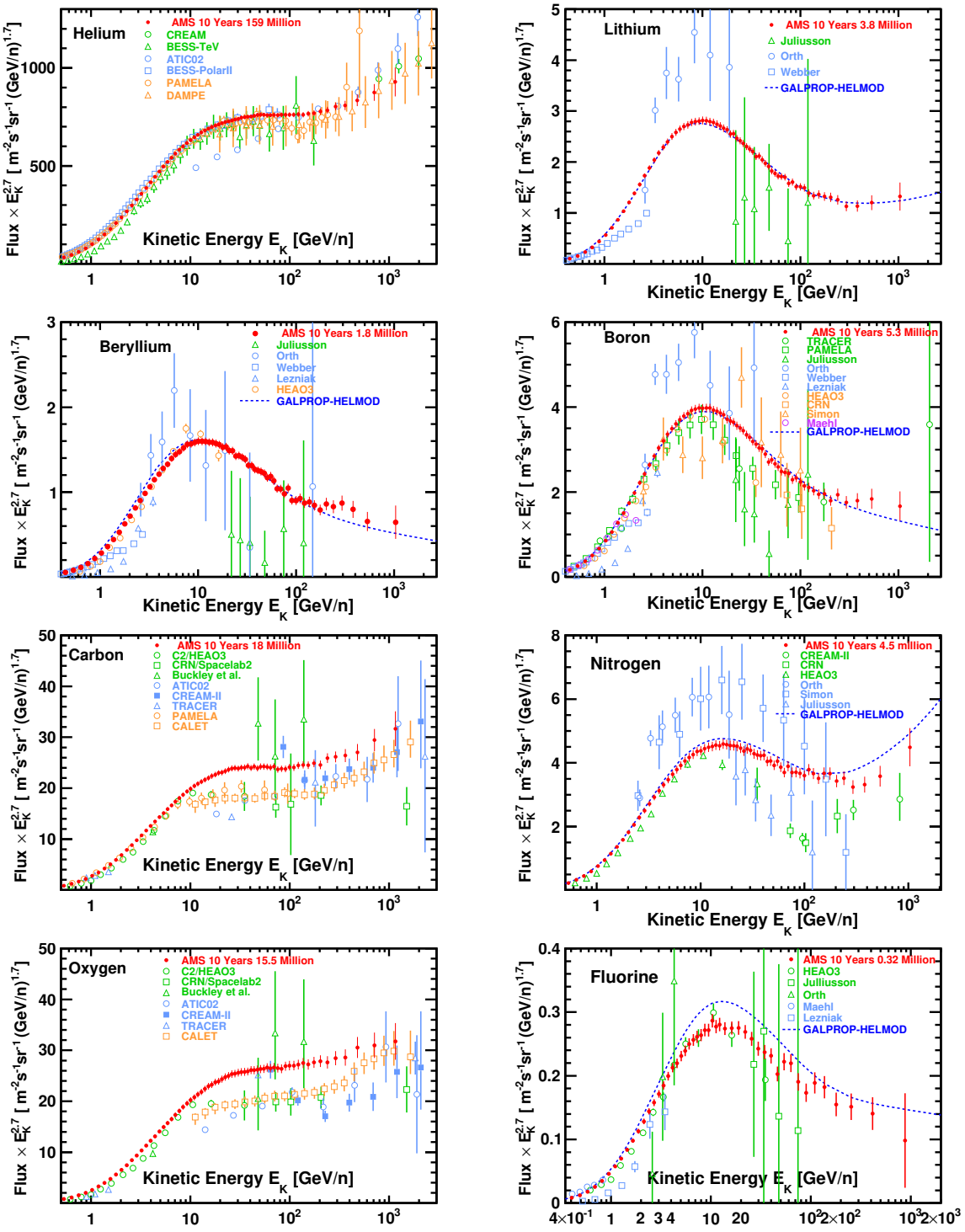

Figure 16: Comparison of the AMS results with other measurements [33, 37–50] and with the predictions of the most recent cosmic ray model GALPROP–HELMOD for Z=2–9.

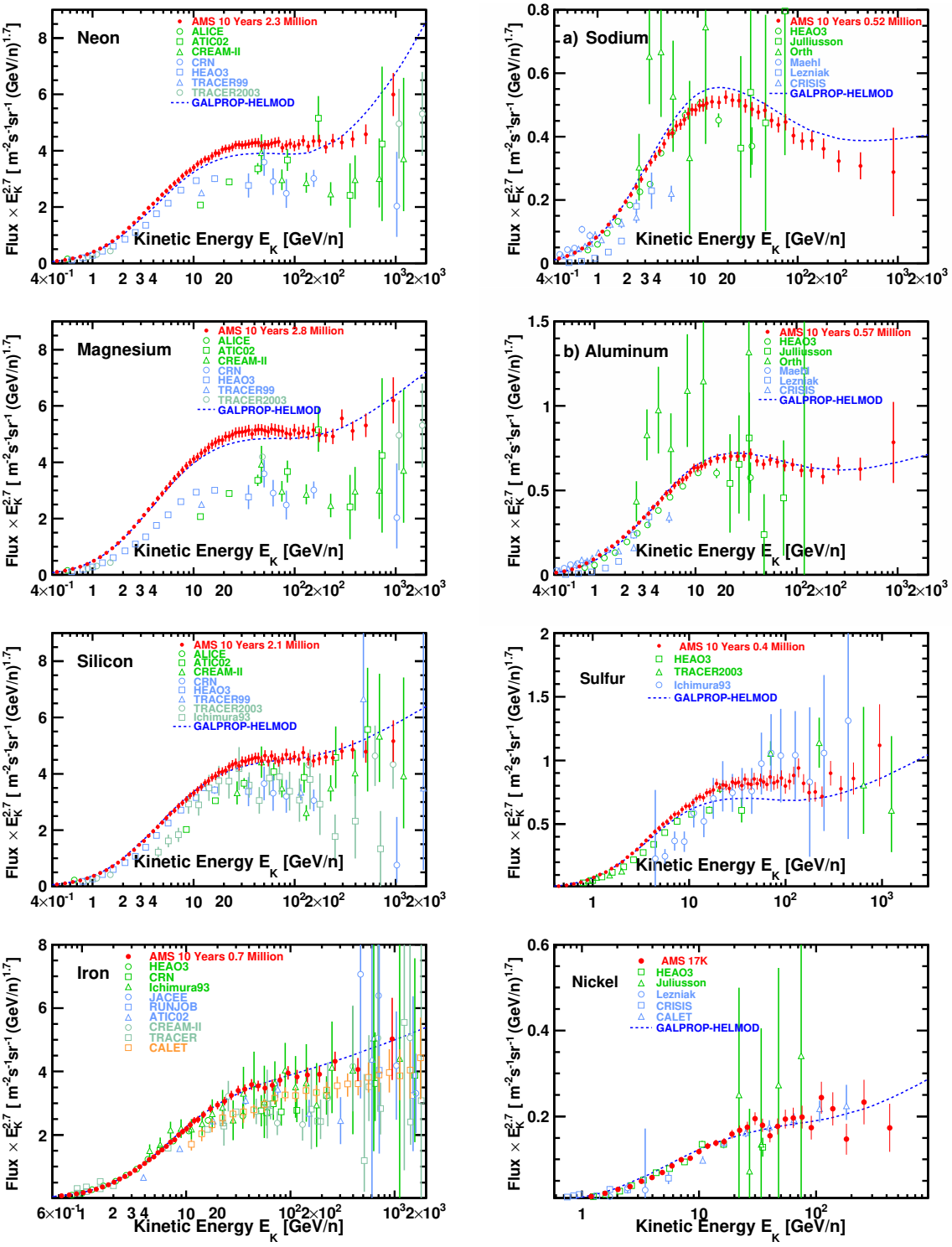

Figure 17: Comparison of the AMS results with other measurements [33, 43, 46, 50–56] and with the predictions of the most recent cosmic ray model GALPROP–HELMOD for Z=10–14, Z=16, Z=26, and Z=28.

A.

Additional error to C/O and N/O abundance ratio due to presence of heavy secondaries in O and B can be estimated as follows. Let us denote

$$\Phi_F = \Phi_F^S;\ \ \Phi_B = \Phi_B^S + a_B \times \Phi_F^S;\ \ \Phi_O = \Phi_O^P + a_O \times \Phi_F^S;\ \ \Phi_{Si} = \Phi_{Si}^P + a_{Si} \times \Phi_F^S \tag{A.1}$$

$$\Phi_C = A_C \times \Phi_O^P + B_C \times \Phi_B^S + a_C \times \Phi_F^S;\ \ \Phi_N = A_N \times \Phi_O^P + B_N \times \Phi_B^S + a_N \times \Phi_F^S \tag{A.2}$$

where index ^{S} denotes secondary flux component and index ^{P} primary flux component. From the above we derive

$$\Phi_C = A_C \times \Phi_O + B_C \times \Phi_B + (a_C - A_C \cdot a_O - B_C \cdot a_B) \times \Phi_F \tag{A.3}$$

$$\Phi_N = A_N \times \Phi_O + B_N \times \Phi_B + (a_N - A_N \cdot a_O - B_N \cdot a_B) \times \Phi_F \tag{A.4}$$

From the table 1 we have $A_C = 0.84, B_C = 0.67, A_N = 0.09$, and $B_N = 0.62$. We then estimate $a_N, a_B \approx 1 - 1.5, a_O, a_C \approx 2.5 - 3, a_{Si} \approx 0.4 - 0.5$ from the F, Ne, Na, Mg, Al, and S secondary components from the same table. The numerical substitutions result in

$$\Phi_C = A_C \times \Phi_O + B_C \times \Phi_B - (0.35 \pm 0.25) \times \Phi_F \tag{A.5}$$

$$\Phi_N = A_N \times \Phi_O + B_N \times \Phi_B + (0.20 \pm 0.15) \times \Phi_F \tag{A.6}$$

where the errors reflect the $a_{N,B,O,C}$ possible range. Refitting the Φ_C, Φ_N with the above formula, we noted both χ^2_C and χ^2_N diminish with respect to the original fits, shown in Fig. 13.

Resulting relative value shifts and additional errors are $0.15\% \pm 0.1\%$ for A_C and $-0.6\% \pm 0.5\%$ for A_N and are negligible with respect with total systematic errors.

There is neither additional shifts nor errors to Ne/Si, Na/Si, Mg/Si, Al/Si, and S/Si abundance ratios at the source in this approximation.

B.

To estimate additional error on $\frac{\mathrm{F/Si}}{\mathrm{B/O}}$ rigidity dependence due to presence of heavy secondary components in B, O, and Si fluxes we have fitted $\frac{\mathrm{F^S/Si^P}}{\mathrm{B^S/O^P}}$ with the Eq. (4) with $a_{Si} = 0.4 - 0.5, a_B = 1 - 1.5, a_O = 2.5 - 3$, see Eq. (A.1). This gives an additional error on δ, see Fig. 11 right panel for definition, of ± 0.003 with final result $\delta = 0.052 \pm 0.007$, a $> 7\sigma$ difference from zero.

Acknowledgments

We acknowledge the continuous support from MIT and its School of Science. We are grateful for the support of the DOE Office of Science. We thank the strong support from CERN IT department.

References

[1] M. Aguilar *et al.*, Physics Reports **894** (2021) 1–116.

[2] K. Lübelsmeyer *et al.*, Nucl. Instrum. Methods Phys. Res., Sect. A **654**, 639 (2011).

[3] B. Alpat *et al.*, Nucl. Instrum. Methods Phys. Res., Sect. A **613**, 207 (2010).

[4] V. Bindi *et al.*, Nucl. Instrum. Methods Phys. Res., Sect. A **743**, 22 (2014).

[5] Ph. von Doetinchem *et al.*, Nucl. Phys. B, Proc. Suppl. 197, 15 (2009).

[6] Th. Kirn, Nucl. Instrum. Methods Phys. Res., Sect. A 706, 43 (2013).

[7] M. Aguilar et al., Nucl. Instrum. Methods Phys. Res., Sect. A 614, 237 (2010); F. Giovacchini Nucl. Instrum. Methods Phys. Res., Sect. A 766, 57 (2014).

[8] C. Adloff *et al.*, Nucl. Instrum. Methods Phys. Res., Sect. A 714, 147 (2013).

[9] G. Ambrosi, V. Choutko, C. Delgado, A. Oliva, Q. Yan, and Y. Li, Nucl. Instrum. Methods Phys. Res., Sect. A **869**, 29 (2017).

[10] Y. Jia, Q. Yan, V. Choutko, H. Liu, and A. Oliva, Nucl. Instrum. Methods Phys. Res., Sect. A **972**, (2020).

[11] J. Allison *et al.*, Nucl. Instrum. Methods Phys. Res., Sect. A **835**, 186 (2016); J. Allison *et al.*, IEEE Trans. Nucl. Sci. **53**, 270 (2006); S. Agostinelli *et al.*, Nucl. Instrum. Methods Phys. Res., Sect. A **506**, 250 (2003).

[12] Q. Yan, V. Choutko, A. Oliva, and M. Paniccia, Nuclear Physics A **996** 121712 (2020).

[13] J. Berdugo, V. Choutko, C. Delgado, and Q. Yan, Nucl. Instrum. Methods Phys. Res., Sect. A **869**, 10 (2017); Q. Yan and V. Choutko "Alignment of the Alpha Magnetic Spectrometer (AMS) in space", Eur. Phys. J. C (2023), *in press*.

[14] M. Aguilar *et al.*, Phys. Rev. Lett. **114**, 171103 (2015).

[15] L. J. Gleeson, W. I. Axford, Astrophys. J. **154**, 1101 (1968).

[16] I. G. Usoskin, G. A. Bazilevskaya, G. A. Kovaltsov, J. Geophys. Res. **116** A02104 (2011); K. G. McCracken, J. Beer, J. Geophys. Res. **112** A10101 (2007); I. G. Usoskin, K. Alanko-Huotari, G.A. Kovaltsov,K. Mursula, J. Geophys. Res. **110** A12108 (2005); We have also used more recent data from: `http://cosmicrays.oulu.fi/phi/Phi_mon.txt`.

[17] M. Aguilar *et al.*, Phys. Rev. Lett. **119**, 251101 (2017).

[18] M. Aguilar *et al.*, Phys. Rev. Lett. **124**, 211102 (2020).

[19] M. Aguilar *et al.*, Phys. Rev. Lett. **126**, 041104 (2021).

[20] M. Aguilar *et al.*, Phys. Rev. Lett. **120**, 021101 (2018).

[21] S. Thoudam & J. R. Hörandel, Astron. Astrophys. **567**, A33 (2014); P. Blasi *et al.* Phys. Rev. Lett. **109**, 061101 (2012); N. Tomassetti, Phys. Rev. D **92**, 081301(R) (2015); A. E. Vladimirov *et al.* Astrophys. J. **752**, 68 (2012).

[22] M. Aguilar *et al.*, Phys. Rev. Lett. **126**, 081102 (2021).

[23] M. Aguilar *et al.*, Phys. Rev. Lett. **127**, 021101 (2021).

[24] V Bresci, E Amato, P Blasi, G Morlino, Monthly Notices of the Royal Astronomical Society, Volume 488, Issue 2 (2019).

[25] M. J. Boschini *et al.*, The Astrophysical Journal Supplement Series, **250** (2020); M. J. Boschini *et al.*, The Astrophysical Journal Supplement Series, **913** (2021).

[26] Y. S. Yoon *et al.*, Astrophys. J. 728, 122 (2011).
[27] Y. Shikaze *et al.*, Astropart. Phys. 28, 154 (2007); K. Abe *et al.* ApJ 822 65 (2016).
[28] K.C. Kim *et al.*, Adv.Space Res. 51 (2013).
[29] S. Haino *et al.*, Proceedings of the 28th International Cosmic Ray Conference. July 31-August 7, 2003. Tsukuba, Japan.
[30] Ivanenko I P *et al.*, 1993 Proc. 23rd Int. Cosmic Ray Conf. (Calgary, Canada) 2 17.
[31] Zatsepin V I *et al.*, 1994 Yad. Fiz. 57 684.
[32] Makoto Hareyama *et al.*, 2006 J. Phys.: Conf. Ser. 47 106.
[33] A. D. Panov *et al.*, Bull. Russ. Acad. Sci. Phys. 73, 564 (2009).
[34] O. Adriani *et al.*, Science 332, 69 (2011).
[35] O. Adriani *et al.*, Phys. Rev. Lett. 122, 181102 (2019).
[36] Q. An *et al.*, SCIENCE ADVANCES Vol 5, Issue 9 (2019).
[37] F. Alemanno *et al.*, Phys. Rev. Lett. 126, 201102 (2021).
[38] E. Juliusson, Astrophys. J. **191**, 331 (1974).
[39] C.D. Orth *et al.*, Astrophys. J. **226**, 1147 (1978).
[40] W. R. Webber & S. M. Yushak, 16th International Cosmic Ray Conference, **12**, 51 (1979).
[41] Lezniak & Webber, Astrophys. J. **223**, 676 (1978).
[42] J. Buckley, J. Dwyer, D. Muller, S. Swordy, and K. K. Tang, Astrophys. J. 429, 736 (1994).
[43] Engelmann et al., Astron. Astrophys. **233**, 96 (1990).
[44] Maehl et al., ApSS 47, 163 (1977).
[45] Simon et al., Astrophys. J. **239**, 712 (1980).
[46] Swordy et al., Astrophys. J. **349**, 625 (1990).
[47] Obermeier et al., Astrophys. J. **724**, 14 (2011).
[48] O. Adriani *et al.*, Astrophys. J. **ApJ** 791, 93 (2014).
[49] O. Adriani *et al.*, Phys. Rev. Lett. 125, 251102 (2020).
[50] H. S. Ahn *et al.*, Astrophys. J. **715**, 1400 (2010); H. S. Ahn *et al.*, Astrophys. J. **714**, L89 (2010); H. S. Ahn *et al.*, Astrophys. J. **707**, 593 (2009).
[51] K.A. Lave *et al.*, Astrophys. J. **770**, 117 (2013); J.A. Esposito *et al.*, Astroparticle Physics **1**, 33 (1992); M. Ichimura *et al.* Phys. Rev. D **48**, 1949 (1993).
[52] F. Gahbauer, G. Hermann, J. R. Hörandel, D. Müller, and A. A. Radu, Astrophys. J. **607**, 333 (2004).
[53] M. Ave, P. J. Boyle, F. Gahbauer, C. Höppner, J. R. Hörandel, M. Ichimura, D. Müller, and A. Romero-Wolf, Astrophys. J. **678**, 262 (2008).
[54] J. Young *et al.*, Astrophys. J. **246**, 1014 (1981).
[55] O. Adriani *et al.*, Phys. Rev. Lett. 126, 241101 (2021).
[56] O. Adriani *et al.*, Phys. Rev. Lett. 128, 131103 (2022).